Materials and Design 160 (2018) 538–548

Contents lists available at ScienceDirect

Materials and Design

journal homepage: www.elsevier.com/locate/matdes

Structural transformation and property improvement of $Fe_{78}Si_9B_{13}$ amorphous ribbon by pulsed laser processing

L.Y. Guo [a], S.N. Geng [b], J. Pang [c], Y.H. Hu [a], S. Lan [d], C.M. Wang [e], W.M. Wang [a,*]

[a] Key Laboratory for Liquid-Solid Structural Evolution and Processing of Materials, Ministry of Education, Shandong University, Jinan 250061, PR China
[b] The State Key Laboratory of Digital Manufacturing Equipment and Technology, School of Mechanical Science and Engineering, Huazhong University of Science & Technology, 430074 Wuhan, PR China
[c] Qingdao Yunlu Energy Technology Company Limited, 97 Yanyang Road, Qingdao 266109, PR China
[d] Herbert Gleiter Institute of Nanoscience, School of Materials Science and Engineering, Nanjing University of Science and Technology, 200 Xiaolingwei Avenue, Nanjing 210094, PR China
[e] School of Materials Science and Engineering, Huazhong University of Science & Technology, 430074 Wuhan, PR China

HIGHLIGHTS

- Hybrid microstructure with amorphous-nanocrystalline is discovered in pulsed laser processed $Fe_{78}Si_9B_{13}$ amorphous ribbon.
- Pitting resistance and magnetic properties of $Fe_{78}Si_9B_{13}$ amorphous ribbon are improved after pulsed laser processing.
- An optimal laser power of $P_L = 20$ W is obtained for pulsed laser processing of $Fe_{78}Si_9B_{13}$ amorphous ribbon.

GRAPHICAL ABSTRACT

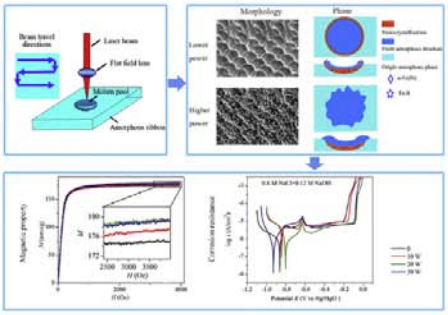

ARTICLE INFO

Article history:
Received 7 June 2018
Received in revised form 25 September 2018
Accepted 27 September 2018
Available online 29 September 2018

Keywords:
Fe-based amorphous ribbon
Pulsed laser processing
Structural transformation
Magnetic property
Pitting resistance
Thermal stability

ABSTRACT

The effects of pulsed laser processing (PLP) with different laser power ($P_L = 10$, 20 and 30 W) on the surface morphology, structure and properties of $Fe_{78}Si_9B_{13}$ amorphous ribbon were investigated. It was found that the circular blobs, convex in perimeter and sunk in middle, distributed regularly on the surface of ribbon after PLP with $P_L = 10$ W. As P_L increased to 20 and 30 W, obvious splashes occurred around the laser blobs. On the surface of ribbons after PLP, fresh amorphous structures were generated, which were confirmed by small angle X-ray scattering and transmission electron microscope data. Meanwhile, a small number of nanocrystallines formed at heat affected zone. The X-ray diffraction results indicated that the transformation from fcc to bcc SRO structure units occurred during PLP, resulting in a lower characteristic distance δ_C. The pitting resistance, soft magnetic property and thermal stability of ribbons were enhanced after PLP. Especially, the properties had a significant improvement with increasing P_L from 10 to 20 W, but had a slight deterioration as P_L increased further from 20 to 30 W. Overall, an optimal laser power of 20 W was obtained for PLP of $Fe_{78}Si_9B_{13}$ amorphous ribbon in this work.

1. Introduction

The amorphous materials are significantly different from the corresponding crystalline alloys due to their disordered and metastable structure, rendering superior properties such as high strength, high

* Corresponding author.
E-mail address: weiminw@sdu.edu.cn (W.M. Wang).

https://doi.org/10.1016/j.matdes.2018.09.045

hardness and excellent corrosion resistance [1,2]. Among various kinds of amorphous alloys, Fe-based amorphous alloys are used widely in power transformers and magnetic sensors, because of their excellent soft magnetic properties, outstanding corrosion resistance and ultra-high strength [3–5].

To further increase the operational efficiency and service life of equipment such as power transformers, many researchers have made great efforts on improving the performance of Fe-based amorphous alloys. The common post-processing methods include annealing [6,7], pressure [8,9], electron beam processing [10] and laser processing [11,12]. Compared with the annealing and pressure, electron beam processing and laser processing can rapidly treat the material in localized manner, which are easier to control the crystallization process of amorphous. Electron beam processing requires vacuum for operation, but laser processing can be operated in atmospheric environment, which is more flexible and easy to operate.

Laser processing utilizes the highly directional, coherent/pulsed, and monochromatic beam to deliver high energy in a localized region on the surface of workpiece [13,14]. It is considered to be an interesting and promising technique for processing amorphous alloys, due to its high heating and cooling rates (10^5–10^8 K/s), which is significantly higher than the critical cooling rate required to produce an amorphous structure for most metallic glasses [15]. In addition, the laser processing is in a non-contact form which could avoid the possible heterogeneous crystallization. Moreover, selective laser melting as an advanced 3D printing technique is particularly attractive owing to its superiority in fabricating complex geometrical features, which has been introduced to the field of bulk metallic glasses to overcome the limitation of glassy forming ability and difficulty in manufacturing [16–19]. During laser processing, the laser beam acts on the surface of material and generates a molten pool and a heat affected zone with a large temperature gradient [20]. The distinct thermal histories could influence the structure evolution in different zone. It have been reported that laser processed amorphous alloy exhibits significant structural heterogeneities: fully amorphous structure in molten pools, whereas a mixture of amorphous phase and nanocrystals in the heat affected zones [17,21,22].

Furthermore, the laser surface treatment can adjust the microstructure of material surface and achieve the desired performance [14]. The research of Joshi [23] was focusing on optimization of laser thermal treatment of Fe–Si–B metallic glass, using a continuous wave to maximize ultimate tensile strength and minimize the electrical resistivity. In Shravana Katakam's research [24], a significant increase in saturation magnetization was observed for laser-treated Fe-Si-B ribbons compared to both as-received and furnace annealed samples. The above studies illustrate that laser processing is effective way to modify the structure and performance of amorphous alloys. Compared to continuous laser, pulsed laser has much higher peak power density and thus larger cooling rate. This indicates that pulsed laser may be more suitable for surface treatment of amorphous alloys. The improvement of mechanical properties of Zr-based bulk metallic glass by pulsed laser surface treatment has been reported [25–27]. However, there is little research about the effect of pulsed laser processing on the structural transformation and corrosion resistance of Fe-based amorphous ribbon.

In the present work, the effects of pulsed laser processing (PLP) with different laser power (P_L) on the surface morphology, structural transformation, thermal stability, corrosion resistance and magnetic properties of $Fe_{78}Si_9B_{13}$ amorphous ribbon have been systematically studied. The connections among the laser power, microstructure and properties have been discussed in this work and an optimal parameter is obtained for PLP of $Fe_{78}Si_9B_{13}$ amorphous ribbon.

2. Experimental

The amorphous ribbons with a nominal composition of $Fe_{78}Si_9B_{13}$ were prepared by a single-roller melt-spinning technique, and they were supplied by Qingdao Yunlu Energy Technology Company, Qingdao, China. The size of the commercial ribbons is 50 mm in width and 30 μm in thickness and we cut the ribbon in proper size for laser processing. The ribbons were processed using the Ytterbium MOPA pulsed fiber laser (TieDan-B50). The type of scanning galvanometer was SACNcube III 14. The laser processing parameters including scan speed, pulse width, power, frequency, track spacing and ring spacing are shown in Table 1. In the present work, the laser power was set as the unique variable, and the values were 10, 20 and 30 W, respectively.

The structure of all the ribbons was examined by X-ray diffraction (XRD, D/Max-rB) with Cu Ka radiation ($\lambda = 0.154056$ nm). SAXS experiments were conducted Anton Parr SAXSpace with Mo target ($\lambda = 0.07117$ nm). The sample chamber was evacuated to vacuum before measurements to reduce the background noise. The scattering patterns were acquired in transmission geometry by a 2D detector. The 2D images were integrated azimuthally, corrected for background scattering and normalized using SAXStreat and SAXSquant software supplied by the vendor (Anton Paar). The resulting scattering intensity $I(Q)$ was plotted as a function of the scattering vector Q. For each sample, we acquired 4 frames data and the acquisition time was 1800 s for each frame. The real space pair distance distribution function $p(r)$ can be obtained by the equation [28]:

$$p(r) = (1/(2\pi^2)) \times \int_0^\infty I(Q)Qr \ \sin(Qr)dr \quad (1)$$

The surface morphology of samples was examined by scanning electron microscopy (SEM, SUPRA55, Zeiss, Germany). The chemical compositions of surface was analyzed by energy dispersive spectroscopy (EDS).Transmission electron microscopy (TEM, JEM-2100) was used to further observe the microstructure of samples. The amorphous ribbons were cut into 3 mm round piece firstly, and then pre-thinned using a single jet electrolytic with 4% perchloric acid and 96% alcohol electrolyte at −20 °C until a hole was formed. Lastly, argon ion thinning was used to obtain the suitable sample for TEM test. The Fourier filtering for HRTEM images was using DigitalMicrograph software.

The magnetic properties were measured by a vibrating sample magnetometer (VSM, JDAW2000D, Yingpu Magnetoelectric Ltd., Changchun, China) under an applied field up to 4000 Oe at room temperature. In order to ensure the accuracy of the results, the magnetization curve measurements were repeated 3 times. The ferromagnetic resonance (FMR) measurements were performed on JEOL JES-FA200 ESR spectrometer with the frequency of 9.05 GHz, microwave power 0.998 mW and modulation frequency of 100 kHz.

The electrochemical measurements were carried out by CHI660E advanced electrochemical workstation with a scanning rate of 1 mV/s at room temperature. There was a typical three-electrode system in electrochemical measurements: working electrode, platinum counter electrode and reference electrode. The electrolyte was 0.6 M NaCl +0.12 M NaOH solution with Hg|HgO reference electrode. In order to ensure the accuracy of the results, the tests were repeated 3 times.

The corroded surface was also analyzed by X-ray photoelectron spectroscopy (ThermoFischer,ESCALAB 250Xi) using Al-Kα X-ray (1486.6 eV). The working potential was 12.5 kV and filament current was 16 mA. The counts were integrated from 10 cycles. The passing energy was 40 eV and step is 0.1 eV. The binding energy was calibrated by using carbon contamination with C 1 s peak (284.6 eV).

Table 1
Parameters for pulsed laser processing.

Number	Speed (mm/s)	Pulse width (ns)	Power (W)	Frequency (kHz)	Tracks spacing (mm)	Ring spacing (mm)
1	3000	200	10	20	0.02	0.1
2	3000	200	20	20	0.02	0.1
3	3000	200	30	20	0.02	0.1

The thermal properties of the ribbons were investigated using differential scanning calorimetry (DSC, Netzsch DSC404) at the continuous heating rates of 10, 20, 30 and 40 °C/min under a flow of high purity argon.

3. Results

3.1. Surface morphologies and microstructure of pulsed laser processed ribbons

The morphologies of as-quenched and PLP ribbons with different P_L are shown in Fig. 1. As can be seen, the surface of as-quenched ribbon is smooth and flat (Fig. 1a). After PLP, the surface of ribbons has obvious laser processed trace and the surface morphologies of ribbons after PLP with different P_L show significantly different. For the ribbon after PLP with $P_L = 10$ W, the circular blobs, which are convex in perimeter and sunk in the middle, distribute regularly on the surface (Fig. 1b). The average radius of blobs is approximately 30 μm. For $P_L = 20$ W, the spreading area of blobs increases and their shape becomes irregular with some splashes around the marginal of blobs (Fig. 1c). For $P_L = 30$ W, more severe splashes are observed around the laser blobs compared with $P_L = 20$ W (Fig. 1d). The EDS results show that the surface of as-quenched ribbon contains approximately 2.41 at.% O, 10.62 at.% Si and 86.97 at.% Fe. For the ribbons after PLP, O content has a significant rise (8–15 at.%) compared with as-quenched ribbon. The spatter droplets have a higher O content. Meanwhile, Si content has an increase after PLP. Especially for $P_L = 20$ W, Si content has an obvious increase up to 12.99 at.%. In addition, the cross-section images of as-quenched ribbon and ribbons after PLP are inserted in the Fig. 1a, b, c and d. For the as-quenched ribbon (left-bottom inset in Fig. 1a), the surface is relatively flat. For the ribbons after PLP (left-bottom insets in Fig. 1b, c and d), the depressed outline of PLP can be clearly observed. Compared with the as-quenched ribbon, the trace of shear band matches the depressed outline of the ribbons after PLP with $P_L = 10$ and 20 W (left-bottom insets in Fig. 1b and c). Especially, the surface of ribbon after PLP with $P_L = 20$ W has an apparent spalling after cutting in SEM specimen preparation. It is speculated that the surface of ribbons after PLP has a layer of fresh amorphous structure with a high brittleness, which will be discussed with the other results in subsequent sections. In addition, the cross-section image of ribbon with $P_L = 30$ W (left-bottom inset in Fig. 1d) has not the obvious spalling, owing to the severe splashes, embrittlement and oxidation on the laser processed surface as well as the removal of spalling in SEM specimen preparation. Furthermore, the EDS results of cross-section images show that Si element tends to concentrate toward the laser processed surface, which is consistent with the EDS result of surface. Moreover, the altitude maps (right-top insets in Fig. 1b, c and d) show an increase of blob depth with the increase of P_L.

The XRD patterns of $Fe_{78}Si_9B_{13}$ ribbons after PLP with different P_L are presented in Fig. 2. Only a broad diffraction peak is observed for all ribbons, indicating that the ribbons maintain a high amorphous phase content after PLP. In order to in-depth analyze the evolution of short range order (SRO) clusters of Fe-based amorphous alloys during PLP, the diffraction peak is fitted with Gaussian method. The top-right inset shows the diffraction peaks after Gaussian fitting, and the bottom-right table lists the center locations $2\theta_{max}$ of the main diffraction peaks. It can be seen that $2\theta_{max}$ of PLP ribbons is higher than that of as-quenched ribbon and increases with increasing P_L. Especially, as P_L increases from 10 to 20 W,their $2\theta_{max}$ increases significantly from 44.62 to 44.74. In addition, the characteristic distance δ_C can be deduced according to following equation [29]:

$$\delta_c = \frac{2\pi}{Q_p} \text{ with } Q_p = \frac{4\pi \sin\theta_{max}}{\lambda} \tag{2}$$

Here, Q_p is the diffraction vector of maximum. λ is the X-ray wavelength. As shown in the inset table of Fig. 2, the characteristic distance δ_C of ribbons after PLP is lower than that of as-quenched ribbon. Moreover, the height of diffraction peaks of ribbons after PLP is lower than that of as-quenched ribbon, implying that the amount of SRO clusters decreases after PLP.

In addition, SAXS was used to study nanoscale structures for $Fe_{78}Si_9B_{13}$ ribbons after PLP, and the results are shown in Fig. 3a. Scatter points are the experimental data and the continuous curves are fitting results. At low Q, all curves show a significant increase of intensity, which is attributed to the scattering from the sample imperfections

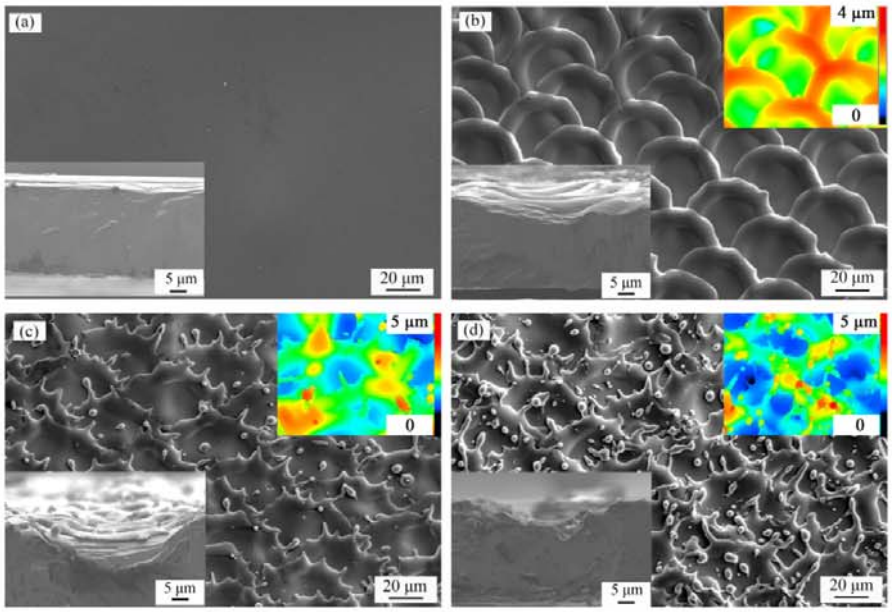

Fig. 1. SEM images of $Fe_{78}Si_9B_{13}$ ribbons: (a) as-quenched ribbon; (b) 10 W, (c) 20 W and (d) 30 W of ribbons after pulsed laser processing. The insets at left-bottom in (a), (b), (c) and (d) are the cross-section images. The insets at right-top in (b), (c) and (d) are the altitude maps.

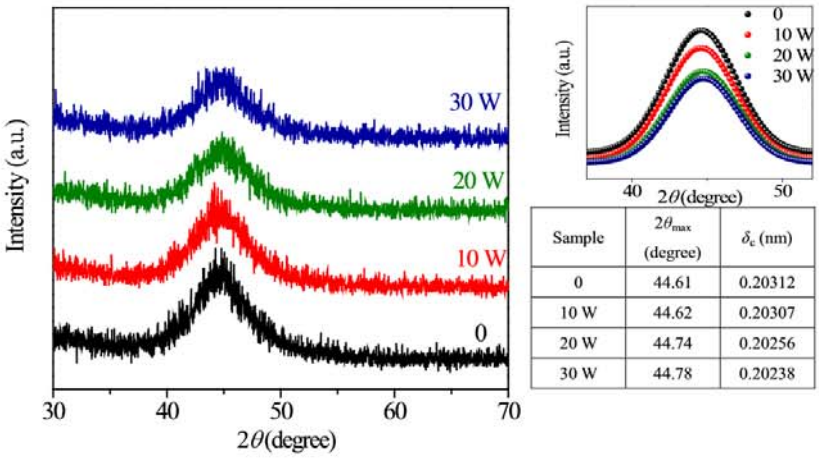

Sample	$2\theta_{max}$ (degree)	δ_e (nm)
0	44.61	0.20312
10 W	44.62	0.20307
20 W	44.74	0.20256
30 W	44.78	0.20238

Fig. 2. XRD patterns of $Fe_{78}Si_9B_{13}$ ribbons after pulsed laser processing with different power. The top-right inset shows the diffraction peaks after Gaussian fitting, and the bottom-right inserted table lists the center locations $2\theta_{max}$ of the main diffraction peaks.

[30]. The intensity of ribbons after PLP at low Q (<1 nm^{-1}) has an obvious increment compared with as-quenched ribbon. The higher P_L the ribbon is treated, the higher SAXS intensity it has. This means that the ribbons after PLP have a higher degree of nanoscale heterogeneities compared with as-quenched ribbon. In addition, the $p(r)$ curves were obtained by indirect Fourier transformation for four ribbons, as shown in Fig. 3b. With increasing P_L, the $p(r)$ peaks tend to shift to the left, indicating that the size of clusters in ribbons tends to decrease with increasing P_L. In particular, it shifts significantly as P_L increases from 10 to 20 W. However, the ribbon with $P_L = 30$ W has a tendency to recover toward as-quenched ribbon.

Moreover, the results obtained from SAXS data seem to have a little difference from that of XRD data, which may be caused by the difference of experiment principle. The examination of XRD focuses on the surface structure transformation, but the SAXS test can penetrate the sample to get the information as a whole. There is a heat affected zone underneath the molten layer of ribbon during PLP, so the structures at the surface and interior have a little difference. The detailed information of the heterogeneous structure is discussed combined with the TEM results in subsequent sections.

Fig. 4 shows the TEM results of as-quenched $Fe_{78}Si_9B_{13}$ amorphous ribbon and ribbons after PLP with different P_L. This contains the bright-field image, selected-area electron diffraction (SAED) pattern and HRTEM image. It is known that Fourier filtering can be applied to highlight the periodicities of certain spacing and direction, and the selected areas in HRTEM images (Fig. 4b, d, f and h) have been Fourier filtered as shown in the inset. For the as-quenched ribbon, the bright-field image (Fig. 4a) shows an almost completely disorder structure, and the corresponding SAED pattern displays the diffused diffraction rings. Meanwhile, the inset in Fig. 4b shows a labyrinth-shape, which is typical amorphous structure. This indicates that the as-quenched ribbon has a fully amorphous structure. For the ribbons after PLP, the TEM images can be observed with two types: amorphous structure and nano-crystalline structure. In the bottom-left parts of Fig.4c, e and g, the bright field images of the matrix of the ribbon after PLP show a fully amorphous character. However, the SAED patterns of ribbons after PLP with $P_L = 20$ and 30 W have an inner halo beside the major halo (top-left parts of Fig.4e and g), implying that $Fe_{78}Si_9B_{13}$ glassy ribbons form a fresh amorphous structure with more short- (or medium-) range ordering clusters after PLP. Moreover, the nano-crystallites in the amorphous matrix are confirmed by the obvious dark regions in bright-field images and diffraction spots in SAED patterns (right parts of Fig.4c, e and g). With the increase of P_L, both the number and size of nano-crystalline phases increase. Their size is <20 nm, owing to the very short laser pulse duration (200 ns). For $P_L = 10$ W (Fig.4c), the α-Fe (Si) nano-crystalline phase is discovered by indexing the SAED patterns. Meanwhile, the crystalline interplanar spacing in the inserted filtered lattices (Fig. 4d) is measured as 0.206 nm, which can be labeled as {110} of α-Fe(Si) phase. For $P_L = 20$ W, only the α-Fe(Si) nano-crystalline phase is discovered in Fig.4e, which is similar to the ribbon

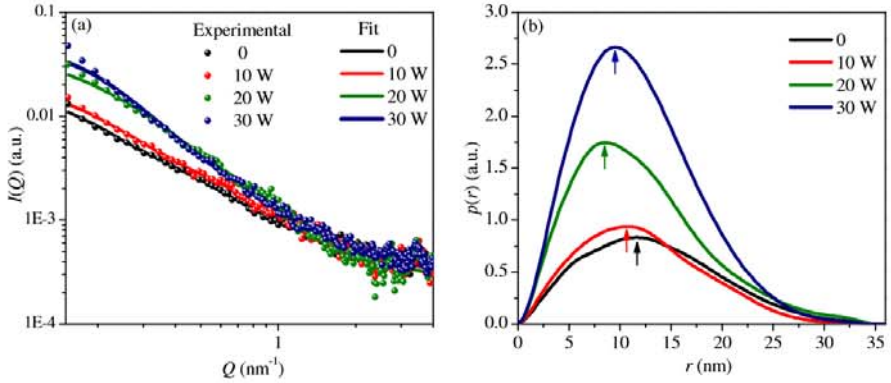

Fig. 3. (a) SAXS data and fitting results of $Fe_{78}Si_9B_{13}$ amorphous ribbons after pulsed laser processing with different power, (b) Pair distance distribution function $p(r)$ curve deduced from the SAXS by indirect Fourier transformation.

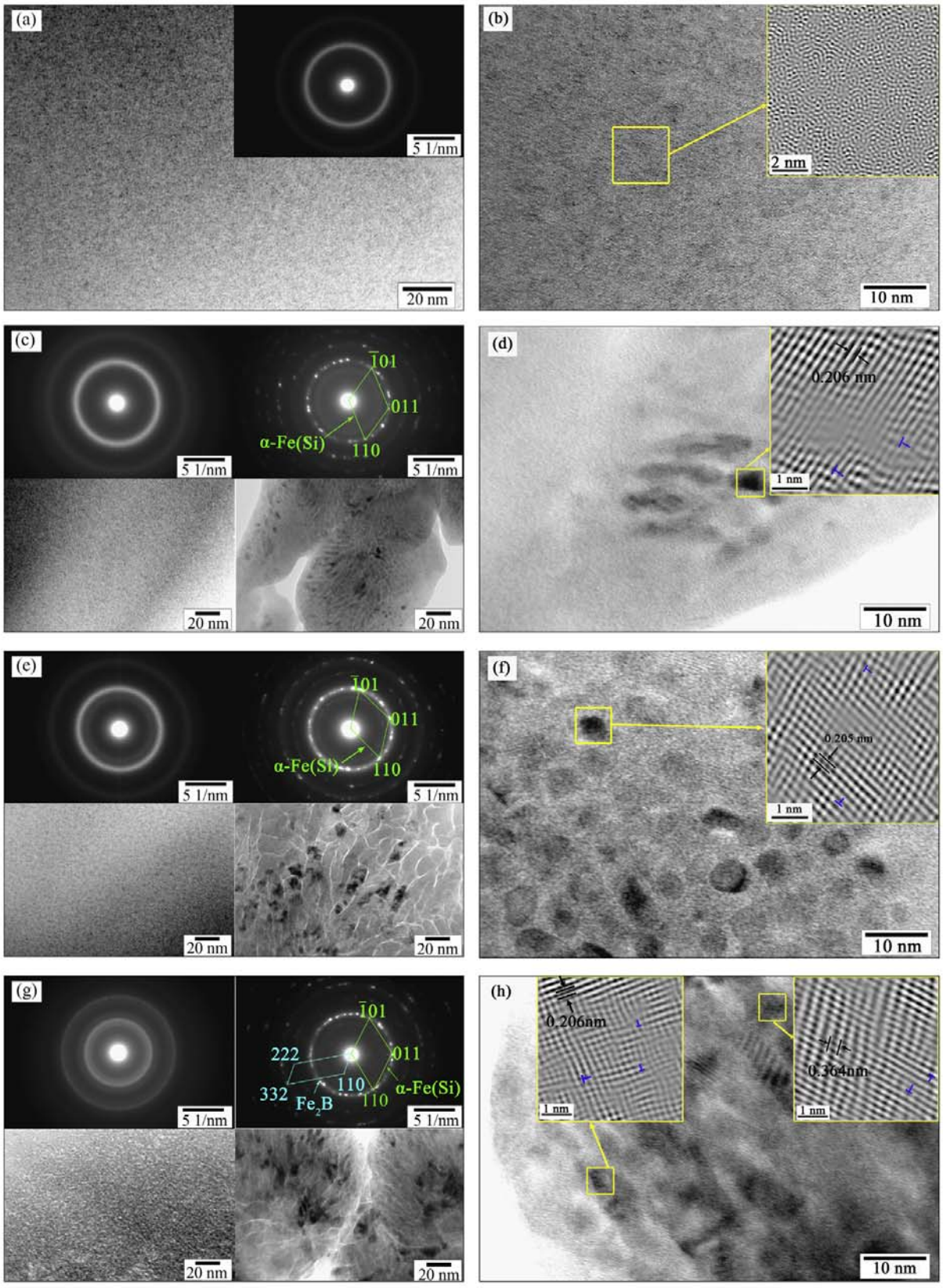
(a)
5 1/nm
20 nm
(b)
2 nm
10 nm
(c)
$\bar{1}01$
011
α-Fe(Si)
110
5 1/nm
5 1/nm
20 nm
20 nm
(d)
0.206 nm
1 nm
10 nm
(e)
$\bar{1}01$
011
α-Fe(Si)
110
5 1/nm
5 1/nm
20 nm
20 nm
(f)
0.205 nm
1 nm
10 nm
(g)
$\bar{1}01$
222
011
332
Fe_2B
110
110
α-Fe(Si)
5 1/nm
5 1/nm
20 nm
20 nm
(h)
0.206nm
0.364nm
1 nm
1 nm
10 nm

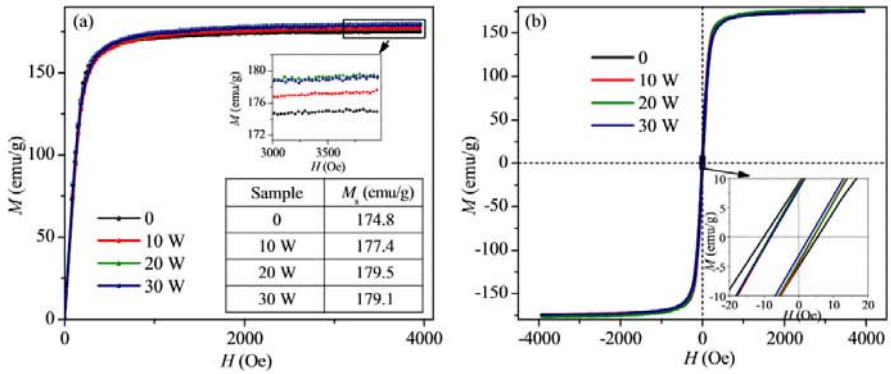

Fig. 5. (a) Magnetization curves and (b) magnetic hysteresis loop for $Fe_{78}Si_9B_{13}$ amorphous ribbons after pulsed laser processing. The top-right inset in (a) shows the larger version of the selected area, and the inserted table in (a) lists the value of saturation magnetization. The inset in (b) shows the larger version of the selected area.

after PLP with $P_L = 10$ W. The crystalline interplanar spacing in the inserted filtered lattices (Fig. 4f) is measured as 0.205 nm, which also can be labeled as {110} of α-Fe(Si) phase. For $P_L = 30$ W (Fig. 4g), Fe_2B crystalline phase can be discovered as well as α-Fe(Si)nano-crystalline phases corresponding with two style lattice arrangement in Fig. 4h. The crystalline interplanar spacings are measured as 0.206 nm and 0.364 nm, which can be labeled as {110} of α-Fe(Si) phase and {110} of Fe_2B phase, respectively. In addition, the dislocation can be found in the filtered lattice, which is related to the residual stress and substitutional solid solution of Si element in α-Fe phase during PLP. Apart from the dark nano-crystallites, the amorphous matrix images of ribbon after PLP have a distinct hybrid structure: gray islands and bright boundary, which is different from the original amorphous phase.

3.2. Magnetic properties of pulsed laser processed ribbons

Fig. 5 shows the magnetization curves and magnetic hysteresis loops of as-quenched $Fe_{78}Si_9B_{13}$ amorphous ribbon and ribbons after PLP with different P_L. With increasing P_L, the M_s of samples tends to increase. As P_L reaches 30 W, the M_s of sample shows a slight decrement (inset in Fig. 5a). In addition, the coercive force H_c of ribbon after PLP is lower than that of as-quenched sample (inset in Fig. 5b). These results indicate that PLP can improve the soft magnetic property of $Fe_{78}Si_9B_{13}$ ribbons.

Fig. 6a shows the FMR spectra of as-quenched $Fe_{78}Si_9B_{13}$ amorphous ribbon and ribbons after PLP with different P_L. The measured spectra curves show two obvious overlapped resonance peaks, suggesting that at least two various magnetic phases or clusters exist in the ribbon. The asymmetry parameter A/B ratio, which reflects the conductivity of the sample, was estimated through the ratio of the intensity of the upper part to that of the lower part of the FMR signals. For the low-conductivity material, the curve is symmetrical with Lorentzian shape (A/B = 1). However, the high-conductivity material exhibits an asymmetric FMR curve (A/B > 1). The A/B ratio increases with the increase of macroscopic conductivity [31]. The A/B ratio of ribbons after PLP is larger than that of as-quenched ribbon, and it has an increase trendy with increasing P_L, indicating an increase of conductivity after PLP (Fig. 6a).

The integral spectra of FMR spectra for four ribbons are shown in Fig. 6b. With increasing P_L, the integral intensity decrease gradually. Particularly, it has a drastic decline as P_L increases from 10 to 20 W. Meanwhile, the total resonance field H_{res}, i.e., peak position, shift to the left side. The resonance field and saturation magnetization have an inverse relationship [32], that is, a lower resonance field means a higher saturation magnetization, which is consistent with VSM results (Fig. 5a).

The Gaussian fitting peaks for FMR integral spectra of as-quenched sample are shown in top-right inset in Fig. 6b. The fitted Gaussian peaks are denoted as P_1, P_2, P_3 and P_4. According to relevant literatures [33,34], P_1 is related to unknown phase, P_2 corresponds to Fe-Si clusters, P_3 corresponds to the Fe-B clusters and P_4 could be considered as a highly disordered intermediate phase. The Gaussian fitting peaks for FMR integral spectra of ribbon after PLP are analyzed in the same method (the curves are not shown here). The resonance field (H_{res}) and line-width (ΔH) of four Gaussian peaks are listed in Table 2. The resonance field (H_{res}) of magnetic phases has a certain shift for different samples, which is due to the change of the magnetic exchange coupling that exists among the various magnetic phases [35]. The H_{res} of P_2 and P_3 has a decrease trend after PLP, confirming a higher saturation magnetization of ribbon after PLP as discussed above. After PLP, the ΔH of P_2 and P_3 peaks has a tendency to increase. Moreover, the ΔH of P_3 peak has a significant rise as P_L increases from 10 to 20 W, but has a slight decrease as P_L increases from 20 to 30 W. The linewidth of the peaks (ΔH) contains information about magnetic inhomogeneities and sample crystallinity as well as the intrinsic relaxation processes in magnetic samples [36].

3.3. Potentiondynamic behavior of pulsed laser processed ribbons

Fig. 7 shows the potentiodynamic polarization curves and parameter variations of as-quenched $Fe_{78}Si_9B_{13}$ amorphous ribbon as well as the ribbons after PLP with different P_L in alkaline solution (0.6 M NaCl +0.12 M NaOH). Each curve has an obvious current plateau which is associated with the passive film formation during the anodic polarization. The first transient passive region at relatively low potentials is a pseudo-passive process, which is related to the active dissolution of metals and formation of low valence oxide [37]. The effect of OH^- on the anodic polarization behavior cannot be ignored due to its strong reactivity even at such low concentrations. Generally, the hydro-ligand MOH_{ads} (M represents a metal) is considered as the precursor in the dissolution process and the interface/interphase film development process [38]. The equation for the low valence oxide formation reaction can be written as [39] $Fe^{2+} + 2OH^- \rightarrow Fe(OH)_2 + 2e^-$. The large passive current density for anodic peaks appear at −0.7 $V_{Hg/HgO}$ in Fig. 7a, indicating the formation and dissolution of $Fe(OH)_2$ and it transforms into Fe_2O_3 phase finally. Moreover, the long passive process at relatively higher potentials until E_{pit} is related to the formation of a continuous stable SiO_2 passive layer [40] $Si + 2H_2O \rightarrow SiO_2 + 4H^+ + 4e^-$. It can be seen that there is a drastic increase of E_{pit} as P_L increases from 10 to 20 W (Fig. 7b).

Fig. 4. TEM images and selected-area diffraction patterns of $Fe_{78}Si_9B_{13}$ amorphous ribbons: (a) (b) as-quenched ribbon; (c) (d) 10 W, (e) (f) 20 W and (g) (h) 30 W of ribbons after pulsed laser processing. The insets in (b), (d), (f) and (h) are the Fourier transformation images of selected area in HRTEM images.

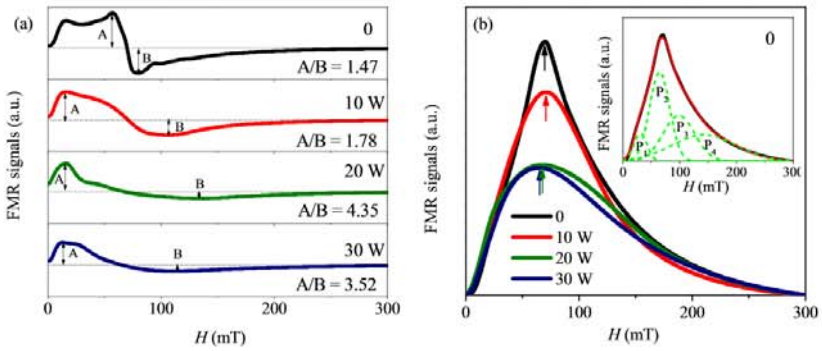

Fig. 6. (a) FMR spectra and (b) integral spectra of FMR spectra for $Fe_{78}Si_9B_{13}$ glassy ribbons after pulsed laser processing. The inset in (b) shows the Gaussian fitting curves for integral spectra of as-quenched $Fe_{78}Si_9B_{13}$ glassy ribbon.

Fig. 8 gives the SEM micrographs of electrochemically corroded surfaces in alkaline solution for four ribbons. The surface of polarized ribbons has two types of regions: the ring-like, severely corroded region and bare region. Apparently, the area of corroded regions tends to decrease with increasing P_L, and a drastic drop occurs as P_L increases from 10 to 20 W, which is possibly associated with the larger deposition rate of Si on the surface. In addition, there are some cracks on the ribbons after PLP with $P_L = 20$ and 30 W, but not on the ribbons after PLP with $P_L = 0$ and 10 W, indirectly reflecting the better pitting resistance of the former.

The X-ray photoelectron spectra of electrochemically corroded surfaces in 0.6 M NaCl +0.12 M NaOH solution for as-quenched ribbon and ribbon after PLP with $P_L = 20$ W are shown in Fig. 9. The shape of Fe 2p, Si 2p and O 1 s curves has no obvious difference between as-quenched ribbon and ribbon after PLP with $P_L = 20$ W. The XPS spectrum of Si 2p can be decomposed into three peaks: Si, SiO_x and SiO_2 [41]. The O 1s spectrum can also be decomposed into three peaks, corresponding with metal oxide species Fe_xO_y (such as Fe_3O_4, Fe_2O), hydroxide species $Fe(OH)_3$ and SiO_2, respectively [42]. Table 3 shows the fraction of decomposed peaks from XPS spectra as well as total area of Si 2p and O 1 s. The total areas of Si 2p and O 1s of ribbon after PLP with $P_L = 20$ W are larger than those of as-quenched ribbon. Moreover, the ribbon after PLP with $P_L = 20$ W has a larger SiO_2 percentage than as-quenched ribbon.

3.4. Thermodynamic parameters of pulsed laser processed ribbons

To analyze the effect of PLP on crystallization kinetic, the $Fe_{78}Si_9B_{13}$ amorphous ribbons after PLP with different P_L were tested using differential scanning calorimetry (DSC). The DSC curves of as-quenched ribbon and ribbons after PLP with a heating rate of 10 °C/min are shown in Fig. 10. All measured curves involve two exothermal peaks, which are labeled as Peak 1 and Peak 2, corresponding to crystallization processes of α-Fe (Si) and Fe-B, respectively [43]. The inserted table shows their first onset temperature (T_{x1}) and peak temperatures (T_{p1} and T_{p2}). Here, T_{x1}, T_{p1} and T_{p2} show an increasing trend with increasing P_L. Furthermore, the T_{x1}, T_{p1} and T_{p2} at heating rates of 20, 30 and 40 °C/min have been also measured, but the corresponding curves are not shown here.

The activation energy E of the crystallization can be calculated by the Kissinger equation, which can be described as the following [44]:

$$\ln\left(\frac{\beta}{T^2}\right) = -\frac{E}{RT} + C \tag{3}$$

where β is the heating rate, T is the characteristic temperature, R is the universal gas constant and C is a constant. Fig. 10 b, c and d show the Kissinger plot for calculation of activation energies and the inserted table shows the value of E_{x1}, E_{p1} and E_{p2}. It is generally known that the onset and peak temperatures are related to the nucleation and growth process, respectively [45], so the activation energy (E_{x1} and E_p) represents the barriers for nucleation and growth, respectively. With increasing P_L, the E_{x1}, E_{p1} and E_{p2} tend to increase. They have a drastic rise as P_L increases from 10 to 20 W and have a slight decrement as P_L increases from 20 to 30 W, which is similar to the variation of measured saturation magnetization and pitting resistance (Figs. 5 and 7).

4. Discussion

With increasing the laser power density during laser processing, the general thermo-physical interactions between laser and material change generally as the following order: (i) laser heating below the crystallization temperature, (ii) laser melting and rapid resolidification and (iii) thermal ablation [46]. According to the laser power and surface morphology (Fig. 1), the process in this work can be classified into the second category of laser melting and rapid resolidification. As the laser acts on the surface of Fe-based amorphous ribbons, its energy is rapidly converted into heat and results in a significant temperature rise. On the one hand, the amorphous phase on the surface layer can be melted and form a small melting pool. On the other hand, a slight volume of melt on the surface layer can vaporize quickly as the temperature exceeds the vaporization temperature [47]. The metal vapor can trigger a large recoil pressure on the molten pool, which can force the melt flows toward pool edge [48]. It can cause the depression of pool center. In addition, the Marangoni flow induced by the surface tension can take the molten from periphery to center, which prevents the further depression of molten pool [49,50]. The hydrostatic pressure also plays an important role in the morphology evolution, which restraints the fluid collapse [49]. The interaction of above forces during PLP can achieve a dynamic equilibrium and form the regular coronary morphology as observed in Fig. 1b for $P_L = 10$ W. As P_L increases to 20 and 30 W, the surface vaporization becomes much tenser, leading to a larger recoil pressure on the melt pool. This breaks the equilibrium in forces instantaneously, and

Table 2
Resonance field (H_{res}) and line-width (ΔH) for four peaks obtained by calculating FMR experimental results of $Fe_{78}Si_9B_{13}$ glassy ribbons after pulsed laser processing with different power.

Sample	H_{res} (mT)				ΔH (mT)			
	P_1	P_2	P_3	P_4	P_1	P_2	P_3	P_4
0	31.0	64.9	98.8	142.9	23	35	55	113
10 W	31.5	61.7	97.9	140.2	25	45	55	107
20 W	27.3	53.2	93.8	156.5	22	42	71	106
30 W	32.5	58.3	94.7	151.5	27	42	65	114

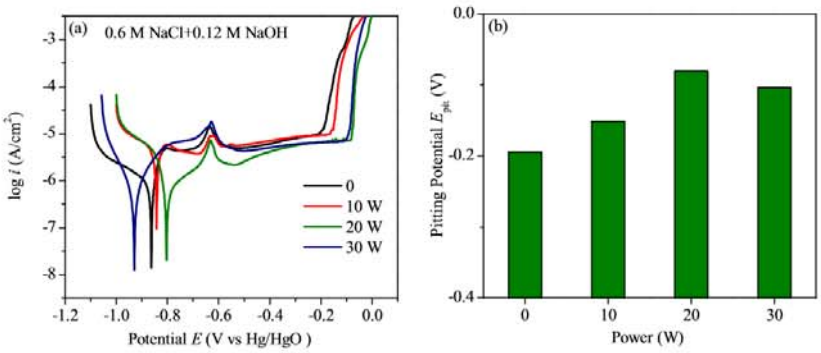

Fig. 7. (a) Potentiodynamic polarization curves (b) variation of pitting potential in 0.6 M NaCl +0.12 M NaOH solution of $Fe_{78}Si_9B_{13}$ glassy ribbons after pulsed laser processing with different laser power.

finally results in the formation of obvious splashes, as can be seen in Fig. 1c and d.

In laser processed materials, there generally exist three zones: the molten zone, which has a very higher temperature and bears the most of the laser beam's energy; the heat-affected zone, where the material stays solid with a large temperature gradient; and the unaffected zone [20,21]. In this work, the material in surface molten zone experiences a high heating and cooling rate during PLP (~10^8 K/s [51]), which is significantly higher than the critical cooling rate as required for Fe-based amorphous alloys [52]. This triggers the formation of new amorphous phase (inset at left-bottom in Fig. 1c). With the increase of depth, the material may not be completely melted due to a short duration time, which promotes the heterogeneous nucleation of the nano-crystalline phase in the re-solidification process. In addition, the crystals can precipitate from the unmelted amorphous matrix in the heat affected zone beneath the melt layer where the temperature reaches a value between the crystallization and melting temperatures of the amorphous alloy. Meanwhile, the unaffected zone maintains the original amorphous structure. Hence, the gradient composite microstructure forms under the distinct thermal histories in different zones induced by PLP.

Based on the above discussion, the evolution of temperature and phase for $Fe_{78}Si_9B_{13}$ amorphous ribbon during PLP can be expressed as a schematic diagram in Fig. 11. Combined with the morphology pictures in Fig. 1, the cases with low and high P_L can be illustrated in Fig. 11b and c. The top surface of Fe-based amorphous ribbons undergoes the highest peak temperature accompanied by the highest heating and cooling rates during PLP. In Fig. 11d and e, the fresh amorphous phase is marked as blue region. The higher P_L is, the larger the blue area is. In addition, the cooling rate during laser processing is larger than that of single-roller melt-spinning technique (~10^6 K/s [53]), so the fresh amorphous structure generated during PLP has a larger degree of disorder than the as quenched glass, which is indicated by a lower cluster diameter in SAXS results (Fig. 3). The increase of fresh amorphous phase can improve the thermal stability of Fe-based ribbons, which is consistent with the higher T_{p1}, T_{p2}, E_{p1} and E_{p2} of ribbon after PLP (Fig. 7).

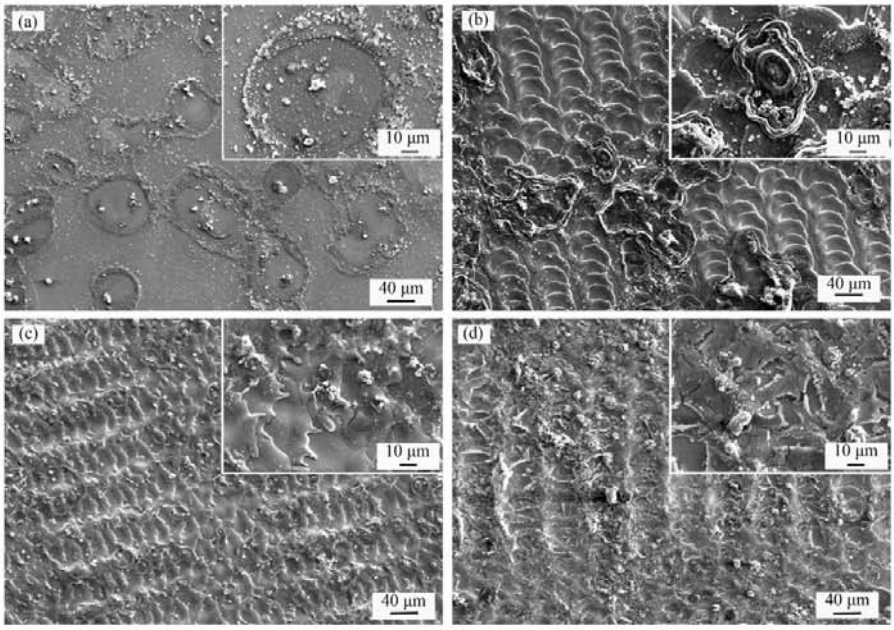

Fig. 8. SEM micrographs of electrochemically corroded surfaces in 0.6 M NaCl +0.12 M NaOH solution for $Fe_{78}Si_9B_{13}$ glassy ribbons: (a) as-quenched ribbon; (b) 10 W, (c) 20 W and (d) 30 W of ribbons after pulsed laser processing.

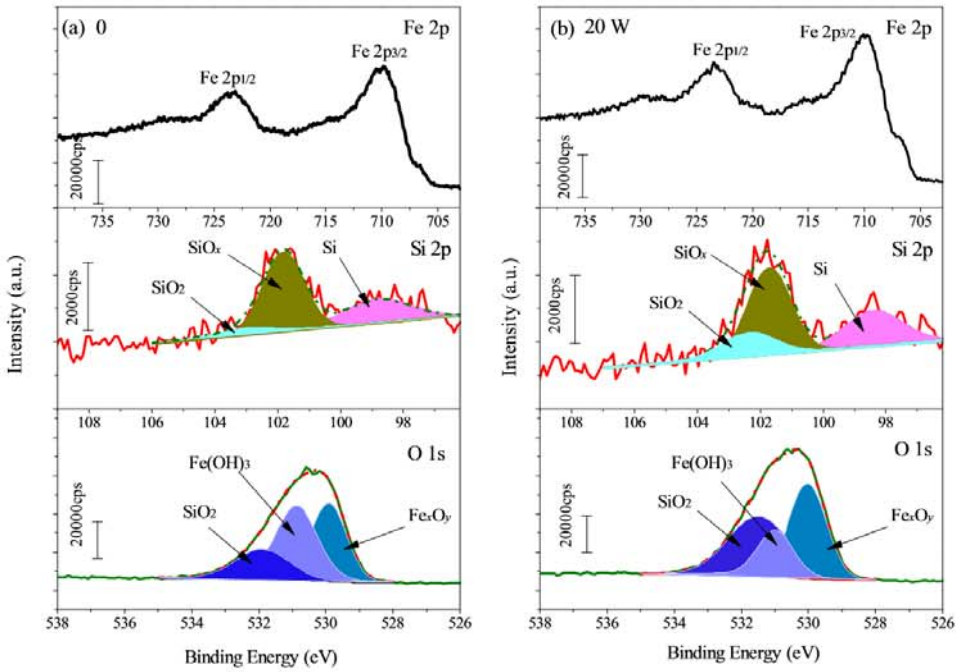

Fig. 9. X-ray photoelectron spectra of electrochemically corroded surfaces in 0.6 M NaCl +0.12 M NaOH solution: (a) as-quenched ribbon and (b) ribbon after pulsed laser processing with $P_L = 20$ W.

Moreover, the lower H_c of ribbon after PLP (inset of Fig. 5b) can be ascribed to the formation of fresh amorphous structures.

In the heat affected zone, the α-Fe(Si) nano-crystalline phases appear in the amorphous matrix at lower P_L as revealed by TEM (Fig. 4), which are marked as diamond-shape in Fig. 11b and c. The area of heat affected zone increases with increasing P_L and its overlap degree increases simultaneously; meanwhile, the susceptibility to crystallization of $Fe_{78}Si_9B_{13}$ glassy ribbons rises. It can explain the precipitation of α-Fe (Si) phase at $P_L = 10$ and 20 W, and the formation of Fe-B phase at $P_L = 30$ W (Fig. 4). Here, Fe-B phases are marked as pentagram-shape in Fig. 11c.

The variation of magnetic property of ribbons after PLP can be expressed as follows combined with the structure transformation. According to two-structure model, iron atoms can exist in the amorphous alloys in the forms of face-centered-cubic/random-closepacked (fcc/rcp) and body-centered-cubic (bcc) structural units simultaneously [29,54]. The fcc structure unit has a denser packing degree and a larger δ_C than bcc structure unit [55]. The characteristic distance δ_C of ribbons decreases after PLP (Fig. 2), indicating that the transformation from fcc to bcc structure units occurs during PLP. On the basis of the Bethe-Slater model [56,57], a denser packing degree results in a lower saturation magnetization M_s, so the M_s of fcc structure units is lower than bcc units. This argument can explain the relation between M_s and δ_C of the samples. Moreover, Fe-B phases are hard magnetic phases [58], which significantly degrade the soft magnetic properties. Therefore, it is understood that the M_s of ribbon with $P_L = 30$ W is lower than that of ribbon with $P_L = 20$ W.

The change of pitting resistance of ribbons after PLP can be ascribed to the change of element contents on the surface and the formation of nano-crystalline phase. Si element plays important role in corrosion resistance of $Fe_{78}Si_9B_{13}$ alloy and it is closely related to the formation of passive layer [40]. The total area of Si 2p and O 1s of ribbon after PLP with $P_L = 20$ W is larger than those of as-quenched ribbon, indicating that there exist more silicon oxides on the surface. Moreover, the ribbon after PLP with $P_L = 20$ W has a larger SiO_2 percentage compared with the as-quenched ribbon, indicating that its protective film of SiO_2 is thicker or denser. Combined with EDS results, it indicates that the higher Si content on surface can form a continuous stable SiO_2 passive layer, leading to an excellent pitting resistance. From this point, the high pitting resistance of the ribbons after PLP can be understood. Moreover, the formation of Fe_2B phase at higher P_L (shown in Fig. 11) can induce the coarsening of the nanocrystals, weaken the Si tunneled effect and passive film formation, which results in the lower E_{pit} of ribbon with $P_L = 30$ W compared with the ribbon with $P_L = 20$ W.

5. Conclusions

In this work, the effects of pulsed laser processing (PLP) with different laser powers (P_L) on the surface morphology, structural transformation, crystallization kinetics, corrosion resistance and magnetic properties of $Fe_{78}Si_9B_{13}$ amorphous alloy were systematically studied.

As $P_L = 10$ W, the circular blobs, which were convex in perimeter and sunk in the middle, distributed regularly on the surface of amorphous ribbon. As $P_L = 20$ and 30 W, obvious splashes were observed around the laser blobs. After PLP, some new fresh amorphous structures were generated at molten zone, which was indicated by SAED patterns. It showed an apparent decrement of the cluster diameter revealed by SAXS data. In addition, nano-crystallites in ribbons after PLP were

Table 3
The fraction of decomposed peaks from XPS spectra as well as total area of Si 2p and O 1s for as-quenched ribbon and ribbon after pulsed laser processing with $P_L = 20$ W.

Sample	Si 2p				O 1s			
	SiO_2 (%)	SiO_x (%)	Si (%)	Total	SiO_2 (%)	Fe $(OH)_3$ (%)	Fe_xO_y (%)	Total
0	12.0	59.3	28.7	6443	20.5	43.3	36.2	145,811
20 W	17.5	52.2	30.3	8315	40.5	19.7	39.8	170,809

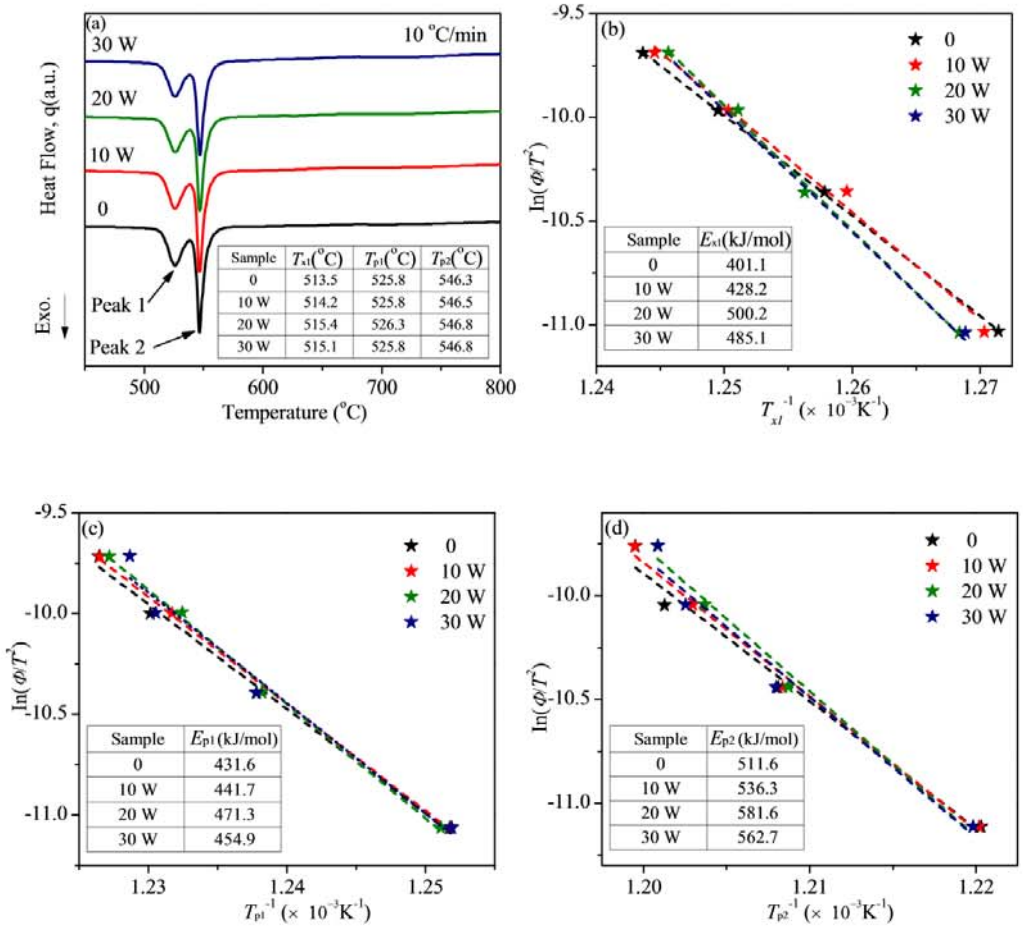

Fig. 10. (a) DSC curves for $Fe_{78}Si_9B_{13}$ glassy ribbons after pulsed laser processing with different power at a heating rate of 10 °C/min and the inserted table lists the value of onset and peak temperatures; ln (β/T_c^2) versus 1000/T_c curves for (b) onset temperature for first peak, (c) first peak temperature and (d) second peak temperature for $Fe_{78}Si_9B_{13}$ glassy ribbons after pulsed laser processing with different power. The inserted tables in (b), (c) and (d) list the value of activation energy.

verified by the TEM. Meanwhile, the transformation from fcc to bcc SRO structure units occurred during PLP, which was suggested by a lower characteristic distance δ_C from XRD parameters. The pitting resistance, thermal stability and magnetic properties of $Fe_{78}Si_9B_{13}$ amorphous ribbons were improved after PLP, especially as P_L increased from 10 to 20 W. However, the properties had a slight decrement as P_L increased from 20 to 30 W, which can be ascribed to the precipitation of Fe_2B phase. Overall, 20 W was an optimal laser power during PLP in this work.

CRediT authorship contribution statement

Lingyu Guo: designed the project, performed the experiments, analyzed the data and wrote the initial draft of the manuscript. **Shaoning**

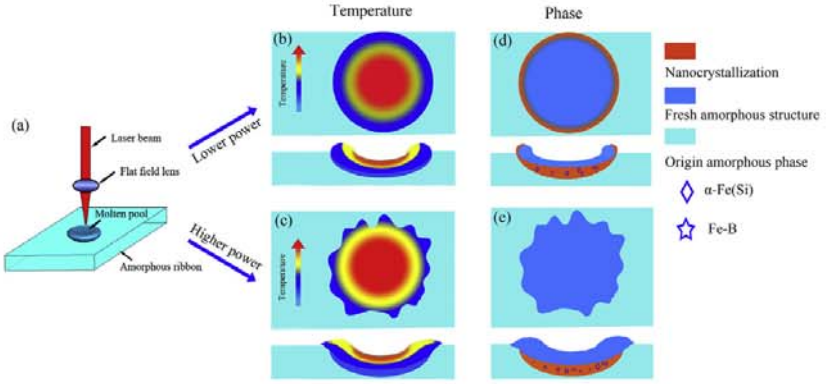

Fig. 11. Schematic of temperature and phase distribution of $Fe_{78}Si_9B_{13}$ glassy ribbons during pulsed laser processing.

Geng: performed the laser experiments and provided assistance on the data analysis. **Jing Pang:** supplied the Fe-based amorphous ribbons. **Yihua Hu:** provided assistance on the VSM test. **Si Lan:** provided help on the SAXS test. **Chunming Wang:** provided assistance on the laser processing technique and data analysis. **Weimin Wang:** made the experimental design and data analysis, and he reviewed and contributed to the final revised manuscript. All authors read the final paper.

Acknowledgement

This work was financially supported by the National Key Research Program of China (2016YFB0300501), Key Research Project of Shandong Province (2016GGX102010) and National Natural Science Foundation of China (51471099, 51571132, 51511140291 and 51771103).

References

[1] F.E. Luborsky, Amorphous Metallic Alloys, Butterworth and Co, London, UK, 1983.
[2] A. Inoue, Stabilization of metallic supercooled liquid and bulk amorphous alloys, Acta Mater. 48 (2000) 279–306.
[3] A. Inoue, B.L. Shen, C.T. Chang, Super-high strength of over 4000 MPa for Fe-based bulk glassy alloys in $[(Fe_{1-x}Co_x)_{0.75}B_{0.2}Si_{0.05}]_{96}Nb_4$ system, Acta Mater. 52 (2004) 4093–4099.
[4] A. Makino, T. Kubota, C. Chang, M. Makabe, A. Inoue, FeSiBP bulk metallic glasses with high magnetization and excellent magnetic softness, J. Magn. Magn. Mater. 320 (2008) 2499–2503.
[5] C.T. Chang, T. Kubota, A. Makino, A. Inoue, Synthesis of ferromagnetic Fe-based bulk glassy alloys in the Fe-Si-B-P-C system, J. Alloys Compd. 473 (2009) 368–372.
[6] Z.B. Zheng, Y.G. Zheng, W.H. Sun, J.Q. Wang, Effect of heat treatment on the structure, cavitation erosion and erosion-corrosion behavior of Fe-based amorphous coatings, Tribol. Int. 90 (2015) 393–403.
[7] G. Herzer, Nanocrystalline soft magnetic materials, Phys. Scr. (1993) (1993) 307.
[8] A. Mari, I.M. Spasojevi, A. Kalezi Gli Ovi, L. Ribi Zelenovi, S. Djuki, N. Mitrovi, The stress effect on electrical resistivity sensitivity of FeBSiC amorphous ribbon, Sens. Actuators, A: Phys. 174 (2012) 103–106.
[9] G. Abrosimova, A. Aronin, D. Matveev, E. Pershina, Nanocrystal formation, structure and magnetic properties of Fe-Si-B amorphous alloy after deformation, Mater. Lett. 97 (2013) 15–17.
[10] Y. Kawamura, Y. Ohno, Successful electron-beam welding of bulk metallic glass, Mater. Trans. 42 (2001) 2476–2478.
[11] S. Katakam, N. Dahotre, Laser patterning of Fe-Si-B amorphous ribbons in magnetic field, Appl. Phys. A Mater. Sci. Process. 117 (2014) 1241–1247.
[12] B.Q. Chen, Y. Li, R. Li, S.J. Pang, Y. Cai, H. Wang, T. Zhang, Influence of laser surface melting on glass formation and tribological behaviors of $Zr_{55}Al_{10}Ni_5Cu_{30}$ alloy, J. Mater. Res. 26 (2011) 2642–2652.
[13] J.D. Majumdar, I. Manna, Laser processing of materials, Sadhana 28 (2003) 495–562.
[14] J.H. Yao, Laser Surface Modification Technology and its Application, National Defence Industry Press, 2012.
[15] F. Audebert, R. Colaço, R. Vilar, H. Sirkin, Production of glassy metallic layers by laser surface treatment, Scr. Mater. 48 (2003) 281–286.
[16] D. Ouyang, N. Li, W. Xing, J.J. Zhang, L. Liu, 3D printing of crack-free high strength Zr-based bulk metallic glass composite by selective laser melting, Intermetallics 90 (2017) 128–134.
[17] D. Ouyang, N. Li, L. Liu, Structural heterogeneity in 3D printed Zr-based bulk metallic glass by selective laser melting, J. Alloys Compd. 740 (2018) 603–609.
[18] Y.Y. Shen, Y.Q. Li, C. Chen, H. Tsai, 3D printing of large, complex metallic glass structures, Mater. Des. 117 (2017) 213–222.
[19] N. Li, J.J. Zhang, W. Xing, D. Ouyang, L. Liu, 3D printing of Fe-based bulk metallic glass composites with combined high strength and fracture toughness, Mater. Des. 143 (2018) 285–296.
[20] B.Q. Chen, Y. Li, Y. Cai, R. Li, S.J. Pang, T. Zhang, Surface vitrification of alloys by laser surface treatment, J. Alloys Compd. 511 (2012) 215–220.
[21] Y.Y. Shen, Y.Q. Li, H. Tsai, Evolution of crystalline phase during laser processing of Zr-based metallic glass, J. Non-Cryst. Solids 481 (2018) 299–305.
[22] G.J. Wu, R. Li, Z.Q. Liu, B.Q. Chen, Y. Li, Y. Cai, T. Zhang, Induced multiple heterogeneities and related plastic improvement by laser surface treatment in CuZr-based bulk metallic glass, Intermetallics 24 (2012) 50–55.
[23] S.S. Joshi, J.Z. Lu, N.B. Dahotre, Optimization of laser thermal treatment of Fe-Si-B metallic glass, J. Manuf. Process. 24 (2016) 31–37.
[24] S. Katakam, A. Devaraj, M. Bowden, S. Santhanakrishnan, C. Smith, R.V. Ramanujan, S. Thevuthasan, R. Banerjee, N.B. Dahotre, Laser assisted crystallization of ferromagnetic amorphous ribbons: a multimodal characterization and thermal model study, J. Appl. Phys. 114 (2013) 184901.
[25] B.Q. Chen, Y. Li, M. Yi, R. Li, S.J. Pang, H. Wang, T. Zhang, Optimization of mechanical properties of bulk metallic glasses by residual stress adjustment using laser surface melting, Scr. Mater. 66 (2012) 1057–1060.
[26] B.Q. Chen, S.J. Pang, P.P. Han, Y. Li, A.R. Yavari, G. Vaughan, T. Zhang, Improvement in mechanical properties of a Zr-based bulk metallic glass by laser surface treatment, J. Alloys Compd. 504 (2010) S45–S47.
[27] L. Zuo, R. Li, Y.Y. Cheng, M.M. Meng, T. Zhang, A. Inoue, Influence of laser surface melting treatment on the surface composition and mechanical properties of a $Zr_{65}Al_{7.5}Ni_{10}Cu_{12.5}Ag_5$ bulk metallic glass, J. Non-Cryst. Solids 488 (2018) 63–68.
[28] A. Guiner, G. Fournet, C.B. Walker, Small Angle Scattering of X-rays, J. Wiley & Sons, New York, 1955.
[29] W.M. Wang, W.X. Zhang, A. Gebert, S. Roth, C. Mickel, L. Schultz, Microstructure and magnetic properties in $Fe_{61}Co_{9-x}Zr_8Mo_5W_xB_{17}$ ($0 \le x \le 3$) glasses and glass-matrix composites, Metall. Mater. Trans. A 40 (2009) 511–521.
[30] X.L. Wu, S. Lan, Z.D. Wu, X.Y. Wei, Y. Ren, H.Y. Tsang, X.L. Wang, Multiscale structures of Zr-based binary metallic glasses and the correlation with glass forming ability, Prog. Nat. Sci. Mater. 27 (2017) 482–486.
[31] G. Tourillon, D. Gourier, F. Garnier, D. Vivien, Electron spin resonance study of electrochemically generated polythiophene and derivatives, J. Phys. Chem. 88 (1984) 1049–1051.
[32] D.C. Estévez, I. Betancourt, Effect of germanium on the microstructure and the magnetic properties of Fe-B-Si amorphous alloys, J. Non-Cryst. Solids 358 (2012) 1778–1782.
[33] X. Wang, H.J. Ma, Z.H. Sheng, S.F. Jin, W. Xu, M. Ferry, L. Chen, J.Q. Duan, W.M. Wang, On the magnetic anisotropy in $Fe_{78}Si_9B_{13}$ ingots and amorphous ribbons: orientation aligning of Fe-based phases/clusters, AIP Adv. 7 (2017), 15302. .
[34] D.S. Schmool, J.S. Garitaonandia, J.M. Barandiaran, Magnetic evolution of the amorphous and nanocrystalline phases and interphase coupling during the crystallization of $Fe_{87}Zr_6B_6Cu$: a ferromagnetic resonance study, Phys. Rev. B 58 (1998) 12159.
[35] D.S. Schmool, J.M. Barandiarán, Ferromagnetic resonance and spin wave resonance in multiphase materials: theoretical considerations, J. Phys. Condens. Matter 10 (1998) 10679.
[36] F. Resonance, S.V. Vonsovskii, Pergamon, Oxford 1966.
[37] M.G. Alvarez, S.M. Vazquez, J. Moya, H. Sirkin, Anodic behaviour of $Fe_{73.5}Si_{13.5-x}Al_xB_9Nb_3Cu_1$ ($x = 0 - 2$) amorphous, nanostructured and crystalline alloys, Scr. Mater. 44 (2001) 507–512.
[38] E. Protopopoff, P. Marcus, P. Marcus, Corrosion Mechanisms in Theory and Practice, Marcel Dekker, New York, 2002 97.
[39] Z.P. Lu, C.B. Huang, D.L. Huang, W. Yang, Effects of a magnetic field on the anodic dissolution, passivation and transpassivation behaviour of iron in weakly alkaline solutions with or without halides, Corros. Sci. 48 (2006) 3049–3077.
[40] I. Chattoraj, K.R.M. Rao, S. Das, A. Mitra, Anodic reactions of amorphous and devitrified Fe-B-Si-Nb-Cu alloys in buffered chloride and fluoride, Corros. Sci. 41 (1999) 1–16.
[41] K. Sato, T. Izumi, M. Iwase, Y. Show, H. Morisaki, T. Yaguchi, T. Kamino, Nucleation and growth of nanocrystalline silicon studied by TEM, XPS and ESR, Appl. Surf. Sci. 216 (2003) 376–381.
[42] Y.J. Li, B. An, Y.G. Wang, Y. Liu, H.D. Zhang, X.G. Yang, W.M. Wang, Severe corrosion behavior of $Fe_{78}Si_9B_{13}$ glassy alloy under magnetic field, J. Non-Cryst. Solids 392-393 (2014) 51–58.
[43] L. Tang, K. Peng, Y.W. Wu, W. Zhang, Effect of ion bombardment on the crystallization kinetics of FeSiNbBCu amorphous alloys, J. Alloys Compd. 695 (2017) 2136–2141.
[44] H.E. Kissinger, Variation of peak temperature with heating rate in differential thermal analysis, J. Res. Natl. Bur. Stand. 57 (1956) 217–221.
[45] H.R. Wang, Y.L. Gao, G.H. Min, X.D. Hui, Y.F. Ye, Primary crystallization in rapidly solidified $Zr_{70}Cu_{20}Ni_{10}$ alloy from a supercooled liquid region, Phys. Lett. A 314 (2003) 81–87.
[46] S.P. Harimkar, S.R. Paital, G. Wang, P.K. Liaw, N.B. Dahotre, Periodically laser patterned Fe-B-Si amorphous ribbons: phase evolution and mechanical behavior, Adv. Eng. Mater. 13 (2011) 955–960.
[47] N.B. Dahotre, S. Harimkar, Laser Fabrication and Machining of Materials, Springer Science & Business Media, 2008.
[48] S.Y. Pang, L.L. Chen, J.X. Zhou, Y.J. Yin, T. Chen, A three-dimensional sharp interface model for self-consistent keyhole and weld pool dynamics in deep penetration laser welding, J. Phys. D. Appl. Phys. 44 (2010), 25301. .
[49] H.Y. Zhao, W.C. Niu, B. Zhang, Y.P. Lei, M. Kodama, T. Ishide, Modelling of keyhole dynamics and porosity formation considering the adaptive keyhole shape and three-phase coupling during deep-penetration laser welding, J. Phys. D. Appl. Phys. 44 (2011), 485302. .
[50] Y.W. Ai, P. Jiang, X.Y. Shao, P.G. Li, C.M. Wang, A three-dimensional numerical simulation model for weld characteristics analysis in fiber laser keyhole welding, Int. J. Heat Mass Transf. 108 ((2017) 614–626.
[51] M. Das, V.K. Balla, D. Basu, S. Bose, A. Bandyopadhyay, Laser processing of SiC-particle-reinforced coating on titanium, Scr. Mater. 63 (2010) 438–441.
[52] H.Y. Jung, S.J. Choi, K.G. Prashanth, M. Stoica, S. Scudino, S. Yi, U. Kühn, D.H. Kim, K.B. Kim, J. Eckert, Fabrication of Fe-based bulk metallic glass by selective laser melting: a parameter study, Mater. Des. 86 (2015) 703–708.
[53] F. Liu, J.Y. Zhang, K. Zhang, Y.Z. Ma, G.C. Yang, The cooling rate quantification and characterization of $Fe_{83}B_{17}$ amorphous ribbon, J. Xi'an Technol. Univ. (2010) 34–39.
[54] W.M. Wang, A. Gebert, S. Roth, U. Kuehn, L. Schultz, Effect of Si on the glass-forming ability, thermal stability and magnetic properties of Fe-Co-Zr-Mo-W-B alloys, J. Alloys Compd. 459 (2008) 203–208.
[55] H. Ino, K. Hayashi, T. Otsuka, D. Isobe, K. Tokumitsu, K. Oda, Appearance of ferromagnetism in fcc solid solutions of binary and ternary Fe-Cu-based systems prepared by mechanical alloying technique, Mater. Sci. Eng. A 304 (2001) 972–974.
[56] R.C.O. Handley, Physics of ferromagnetic amorphous alloys, J. Appl. Phys. 62 (1987) R15–R49.
[57] R. Hasegawa, Magnetic properties of glassy Fe-Be-B alloys, J. Appl. Phys. 52 (1981) 1847–1849.
[58] L. Xue, H.S. Liu, L.T. Dou, W.M. Yang, C.T. Chang, A. Inoue, X.M. Wang, R.W. Li, B.L. Shen, Soft magnetic properties and microstructure of $Fe_{84-x}Nb_2B_{14}Cu_x$ nanocrystalline alloys, Mater. Des. 56 (2014) 227–231.